Supporting Information

Ultralow Iridium-Incorporated Ni-Fe Bimetallic-Organic Framework for Efficient Oxygen Evolution Reaction

Zixiong Wang, Zhaoxin Zhou, Qi Zhang, He Zhu*, Shiping Zhu*

Experimental

Materials: Nickel foam (Jilin Tianxuan Economic and Trade Co. Ltd), 1,4-bis(4*H*-1,2,4-triazol-4-yl)benzene (btz) (Jilin Chinese Academy of Sciences-Yanshen Technology Co., Ltd), anhydrous $FeCl_3$ (Energy-Chemical, 99%), $FeCl_2{\cdot}4H_2O$ (Macklin, 99.9%), $NiCl_2{\cdot}6H_2O$ (Energy-Chemical, 99%), and $IrCl_3{\cdot}xH_2O$ (J&K Scientific, 50-58% Iridium) were used as received without further purification. Dimethyl sulfoxide (DMSO) and ethanol were purchased from Beijing Chemical Works. Ultrapure water was obtained by using a Milli-Q water purification system and used in all experiments. All chemicals and solvents were of analytical grade and used as received without further purification.

Synthesis of NiFe-btz/NF, Ni-btz/NF and Fe-btz/NF electrodes

NF was first washed with water and ethanol to remove the organics on the surface, followed by ultrasonically cleaning in 1 M HCl solution to remove the oxide layer. For the synthesis of NiFe-btz/NF electrode, 0.2 mmol $FeCl_3$ and 0.1 mmol btz were dissolved in 10 mL DMSO/H_2O solution (volume ratio at 2:8) with a 30-minute ultrasonic treatment. Next, a piece of pretreated NF (1 cm × 2 cm) was immersed in the solution and the mixture was transferred into a 30 mL glass vial, which was further heated at 120 ℃ for 4 hours. After cooling down to room temperature, the obtained NiFe-btz/NF was carefully cleaned with water and ethanol and dried at 80 ℃ for 8 hours. The preparation of Ni-btz/NF and Fe-btz/NF was similar to the above process except that for the metal source, $NiCl_2{\cdot}6H_2O$ (0.2 mmol) was used for Ni-btz/NF and $FeCl_2{\cdot}4H_2O$ (0.2 mmol) was used for Fe-btz/NF.

Synthesis of Ir-NiFe-btz/NF, Ir-Ni-btz/NF and Ir-Fe-btz/NF electrodes

2 mg of $IrCl_3{\cdot}xH_2O$ was dissolved in 10 mL deionized water followed by vigorous

stirring for 1 hour to give a homogenous solution. The prepared NiFe-btz/NF was dipped into the solution, and the mixture was transferred to a 20 mL autoclave lined with stainless steel Teflon and heated to 80 ℃ for 12 hours. After cooling down to room temperature, the obtained Ir-NiFe-btz/NF was carefully cleaned with water and ethanol, and dried at 60 ℃ for 8 hours. The same procedure was used to obtain Ir-Ni-btz/NF and Ir-Fe-btz/NF electrodes for comparison.

General Characterizations

Powder X-ray diffraction (PXRD) measurements were conducted using a Rigaku SmartLab X-ray diffractometer with Cu-Kα radiation (40 kV, 30 mA, λ = 1.5418 Å) and a scanning step of 0.01°. X-ray photoelectron spectroscopy (XPS) measurements were performed using a Thermo ESCALAB 250. Scanning electron microscopy (SEM) characterization was performed on an FEI XL-30 ESEM FEG and transmission electron microscopy (TEM) was recorded using a JEOL JEM 2100F. Inductively coupled plasma-optical emission spectroscopy (ICP-OES) measurement was performed on a PerkinElmer 8300. Nitrogen adsorption-desorption experiments were conducted at 77 K using a Quantachrome Autosorb-iQ2 analyzer. NiFe-btz was exchanged with ethanol and then activated at 80 ℃ for 24 hours before the measurement.

Electrochemical Characterizations

Oxygen evolution reaction tests were conducted using a three-electrode cell on a CHI760E electrochemical workstation (Shanghai Chenhua Instrument Co. Ltd) in 1 M KOH (pH=13.8) under the ambient environment. MOF-based electrode (0.5 cm × 1 cm) was used as the working electrode, a platinum plate (1 cm × 1 cm) was used as the counter electrode and Ag/AgCl (3.5 M KCl) was used as the reference electrode. The potentials in the measurements were converted to the reversible hydrogen electrodes (RHEs) scale according to Equation (1):

$$E_{RHE} = E_{Ag/AgCl} + 0.059 \times pH + 0.205 \quad (1)$$

For comparison, a commercial RuO_2 electrode was prepared by dissolving 5 mg RuO_2 in a mixture of 0.98 mL ethanol and 0.02 mL 5 wt% Nafion solution followed by ultrasonication until a homogenous catalyst ink was formed. Then, 0.1 mL suspension was dripped on a clean NF with the same size of 0.5 cm × 1 cm. For each sample, cyclic voltammetry (CV) cycles were conducted in the electrolyte before the linear sweep voltammetry (LSV) at a sweep rate of 50 mV s^{-1} as long as the CV curves reached a steady state. LSV polarization curves were 95% *iR*-corrected and recorded at a scan rate of 5 mV s^{-1}. Tafel plots were computed using Equation (2) obtained from the LSV curves:

$$\eta = a + b \times \log j \quad (2)$$

where η refers to the overpotential, a is a constant, b represents the Tafel slope and j means the current density. The value range of the Tafel lay around 1.6 on the x-axis, corresponding to the current density of 50 mA cm^{-2} for all the prepared catalysts. Electrochemical impedance spectroscopy (EIS) was carried out at 1.55 V versus RHE over a frequency ranging from 100 kHz to 0.1 Hz. The electrochemical active surface area (ECSA) of the working electrode was determined by calculating the double layer capacitance (C_{dl}) via recorded CV curves in the non-Faradaic region between 1.18 and 1.28V versus RHE with varying scan rates (20, 40, 60, 80, 100 mV s^{-1})

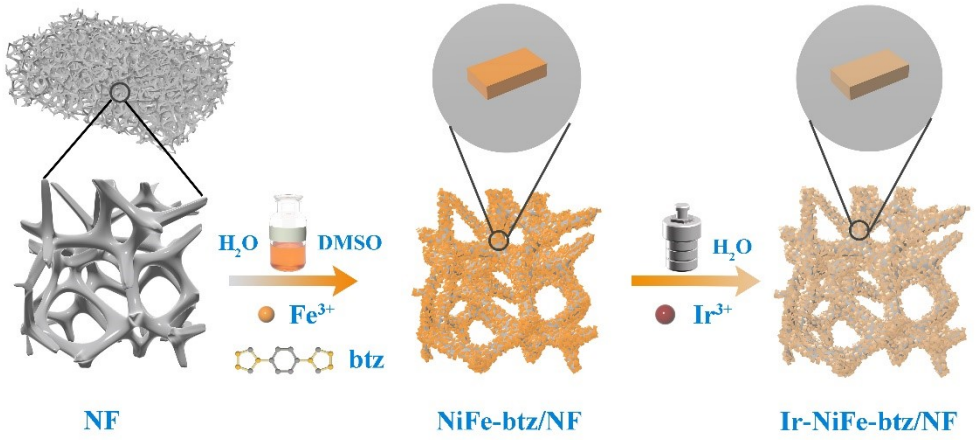

Fig. S1. Schematic illustration of the preparation procedure of Ir-NiFe-btz/NF electrode.

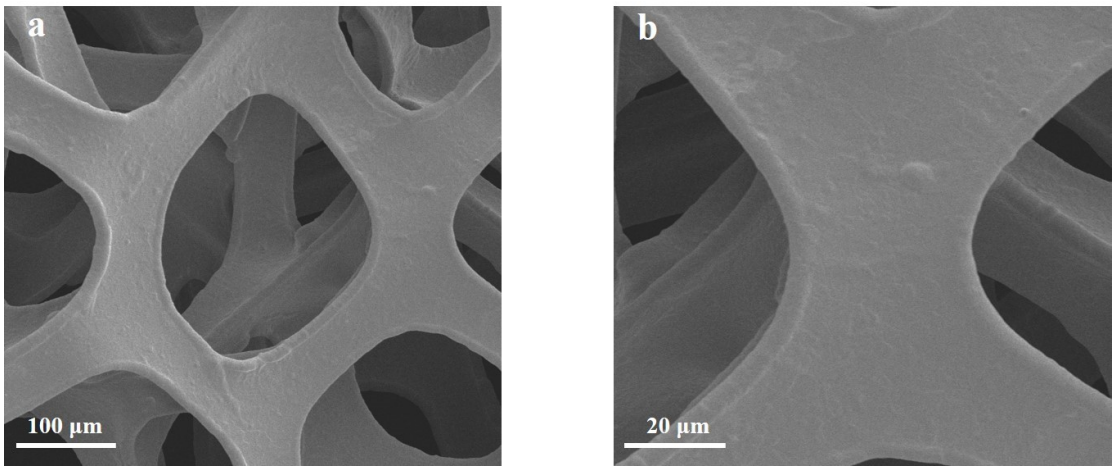

Figure S2. SEM images of pretreated NF substrate.

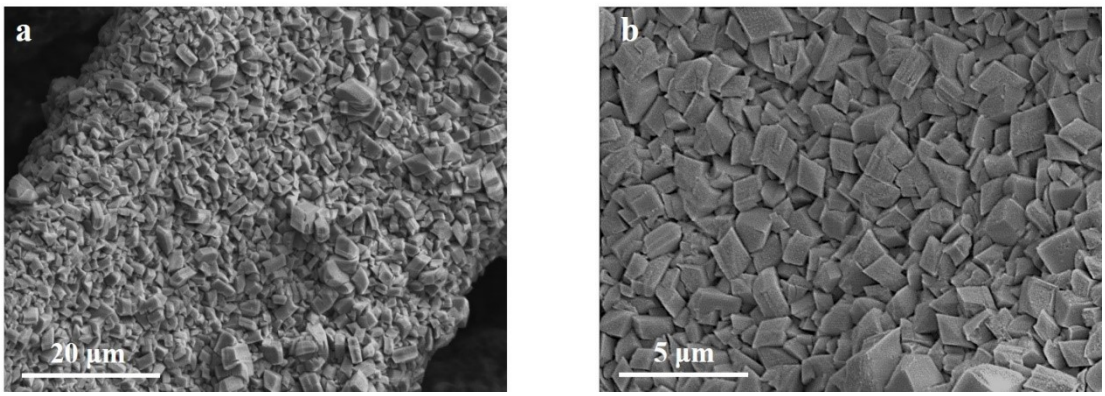

Figure S3. SEM images of NiFe-btz *in situ* grown on NF substrate.

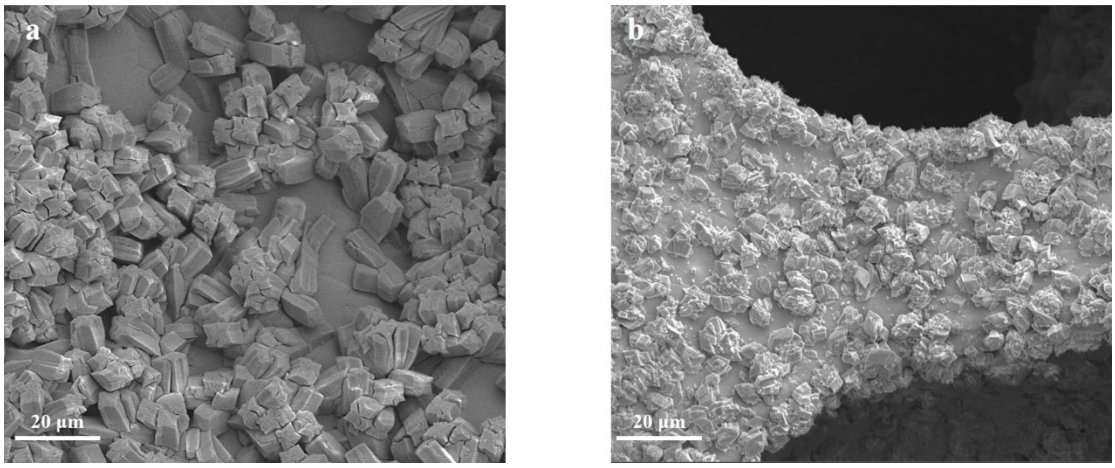

Figure S4. SEM images of monometallic MOF, namely **a)** Ni-btz and **b)** Fe-btz, *in situ* grown on NF substrate.

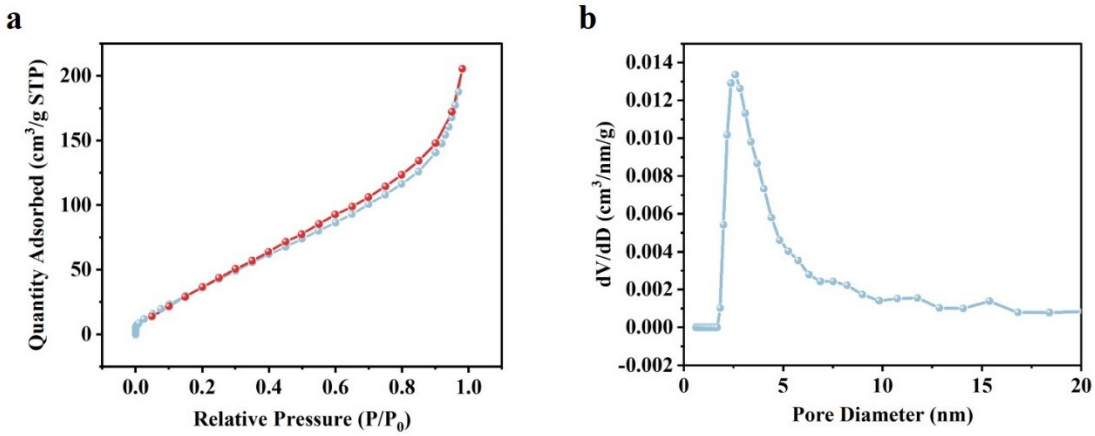

Figure S5. **a)** N_2 adsorption-desorption isotherms of NiFe-btz. **b)** The corresponding pore size distribution plot.

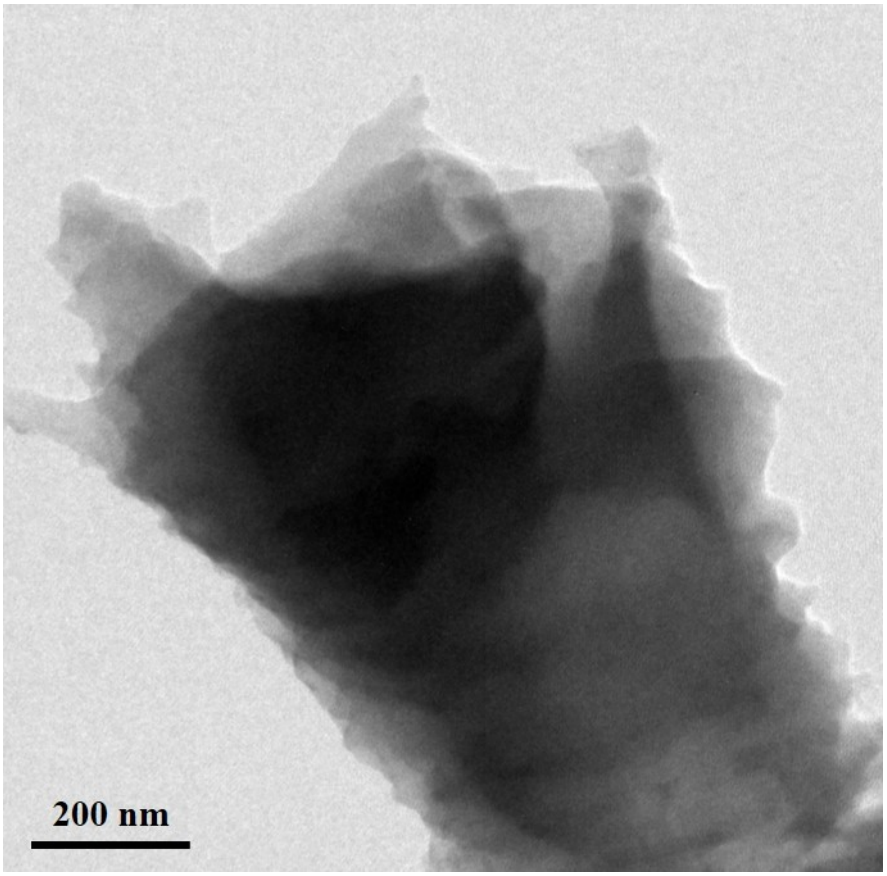

Figure S6. TEM image of NiFe-btz.

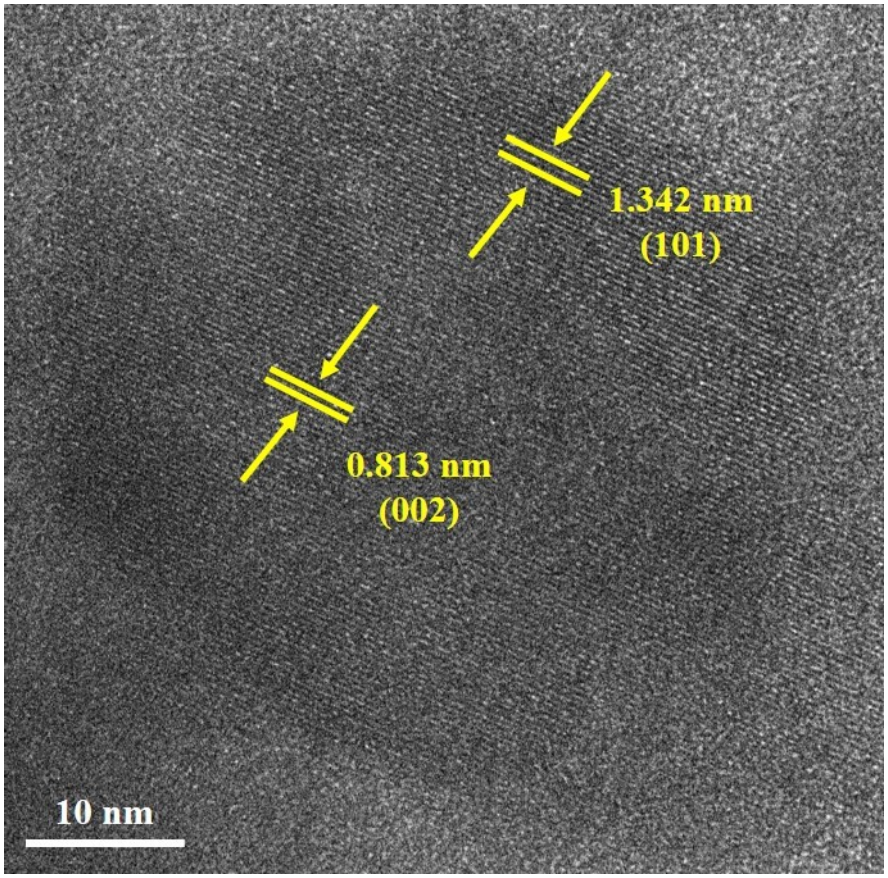

Figure S7. High-resolution TEM image of NiFe-btz showing the lattice spacings and the corresponding crystal planes.

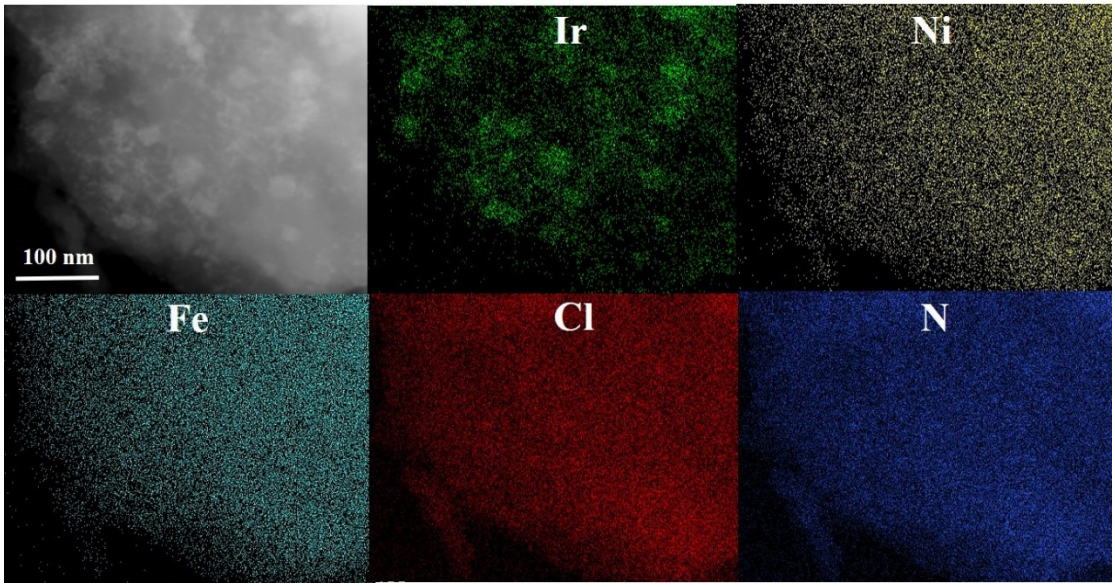

Figure S8. Elemental mappings of important elements of Ir-NiFe-btz.

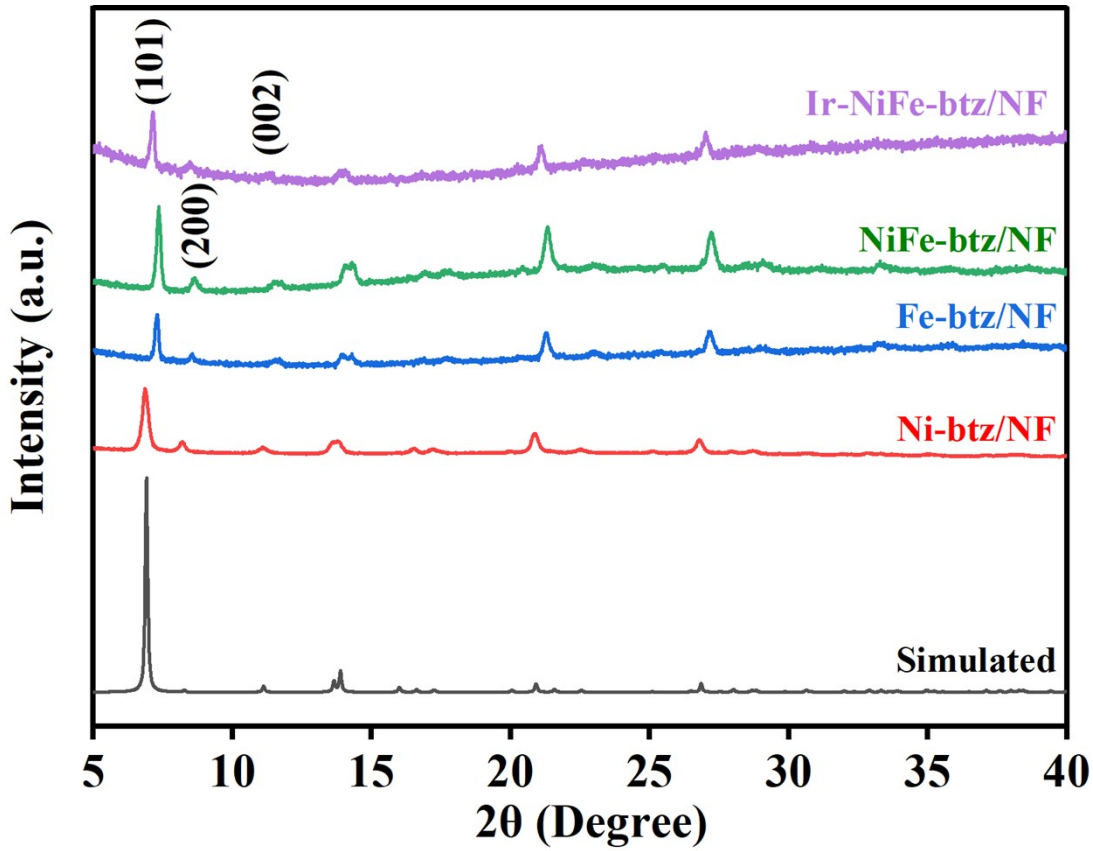

Figure S9. PXRD patterns of as-synthesized MOF electrodes.

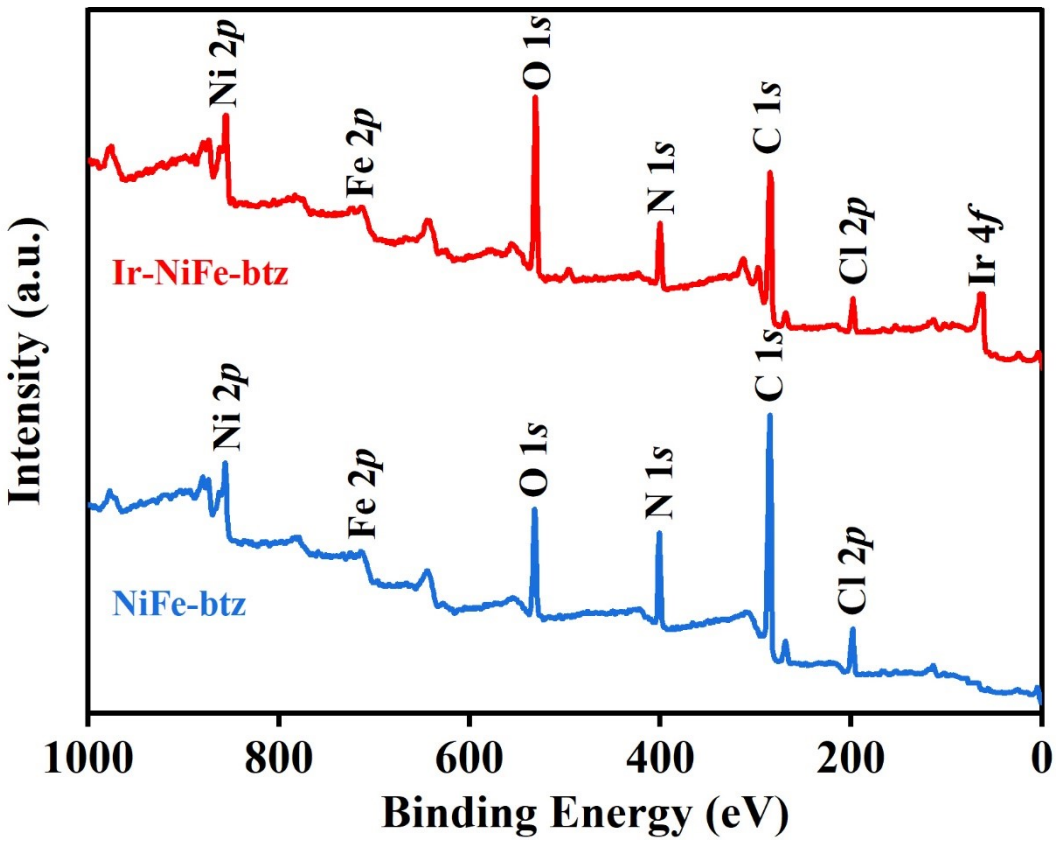

Figure S10. XPS survey spectra of NiFe-btz and Ir-NiFe-btz.

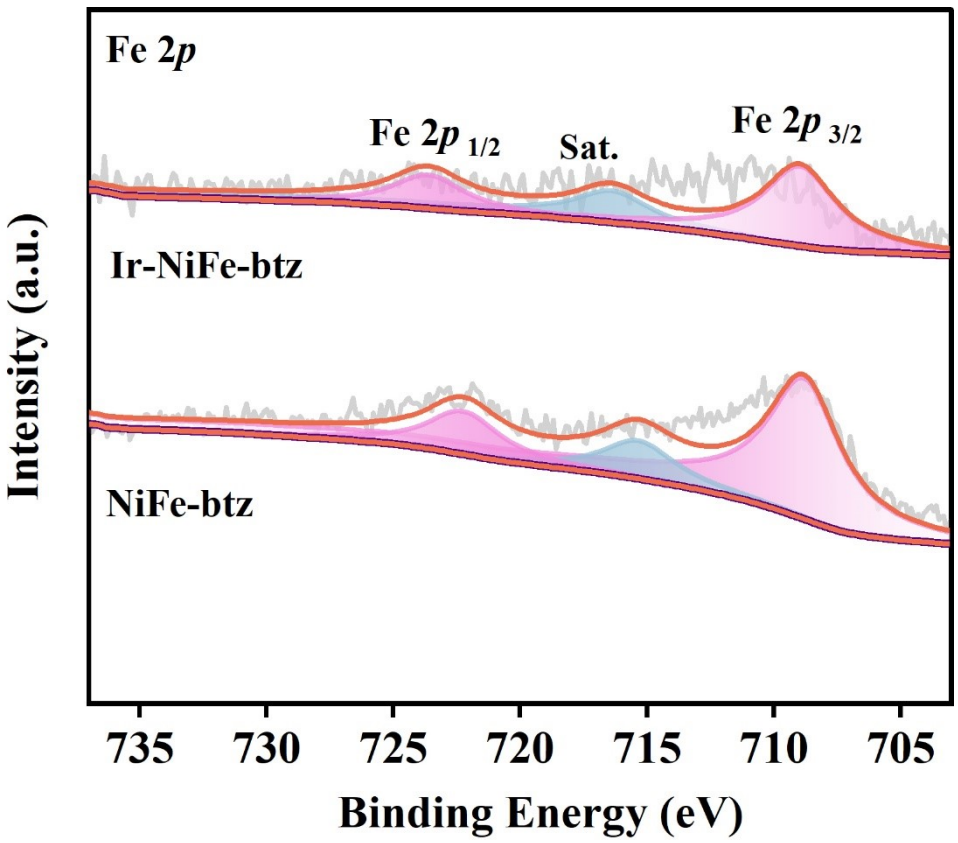

Figure S11. High-resolution XPS spectra of Fe 2*p* in Ir-NiFe-btz and NiFe-btz electrodes.

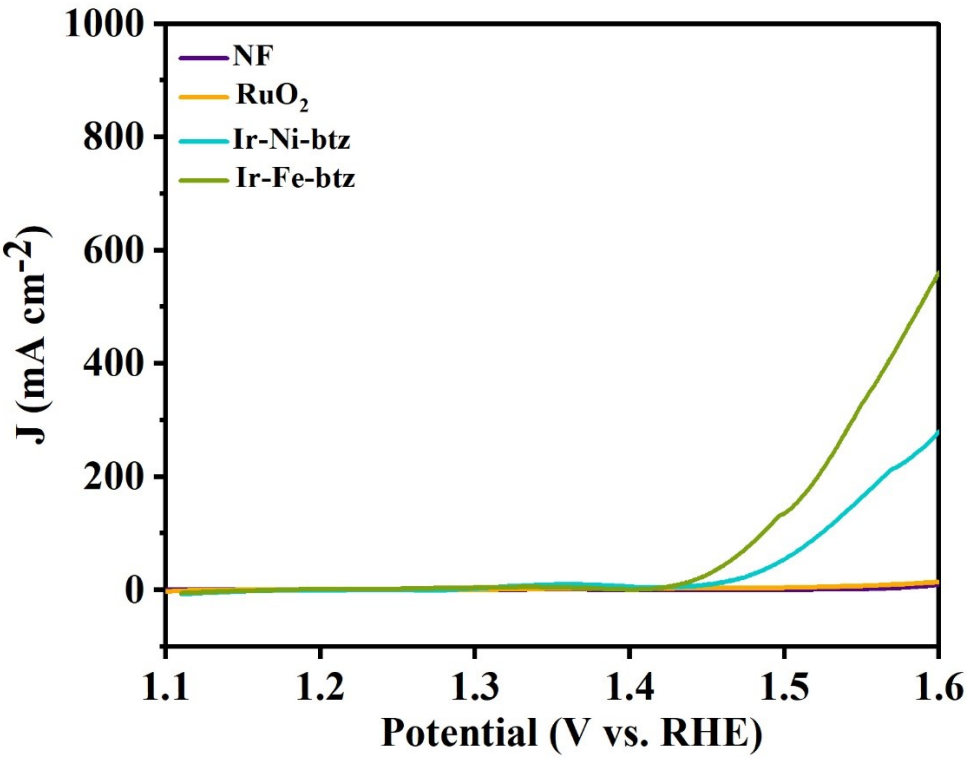

Figure S12. LSV curves of NF, RuO_2, Ir-Ni-btz and Ir-Fe-btz electrodes.

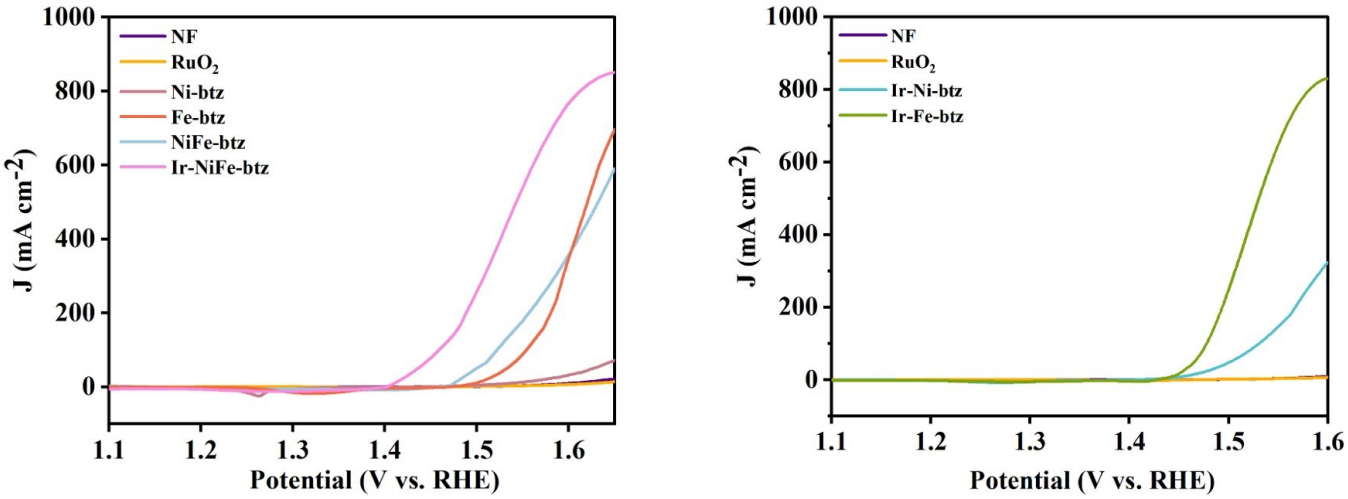

Figure S13. LSV curves of as-synthesized MOF electrodes from the reverse sweep.

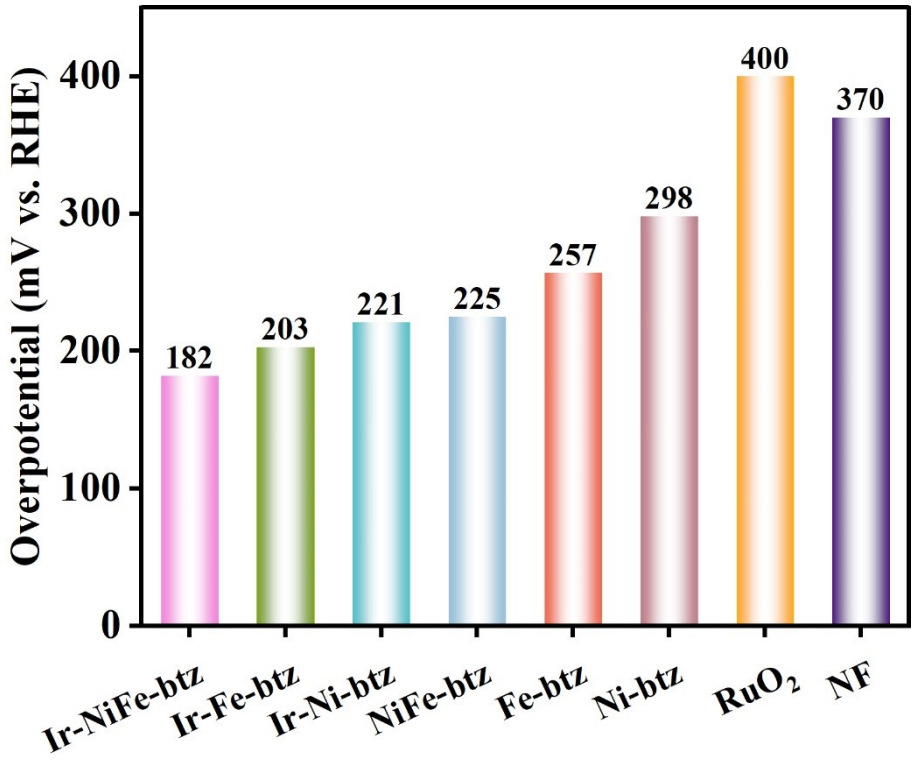

Figure S14. Histograms of the overpotentials at 10 mA cm^{-2} for various electrodes.

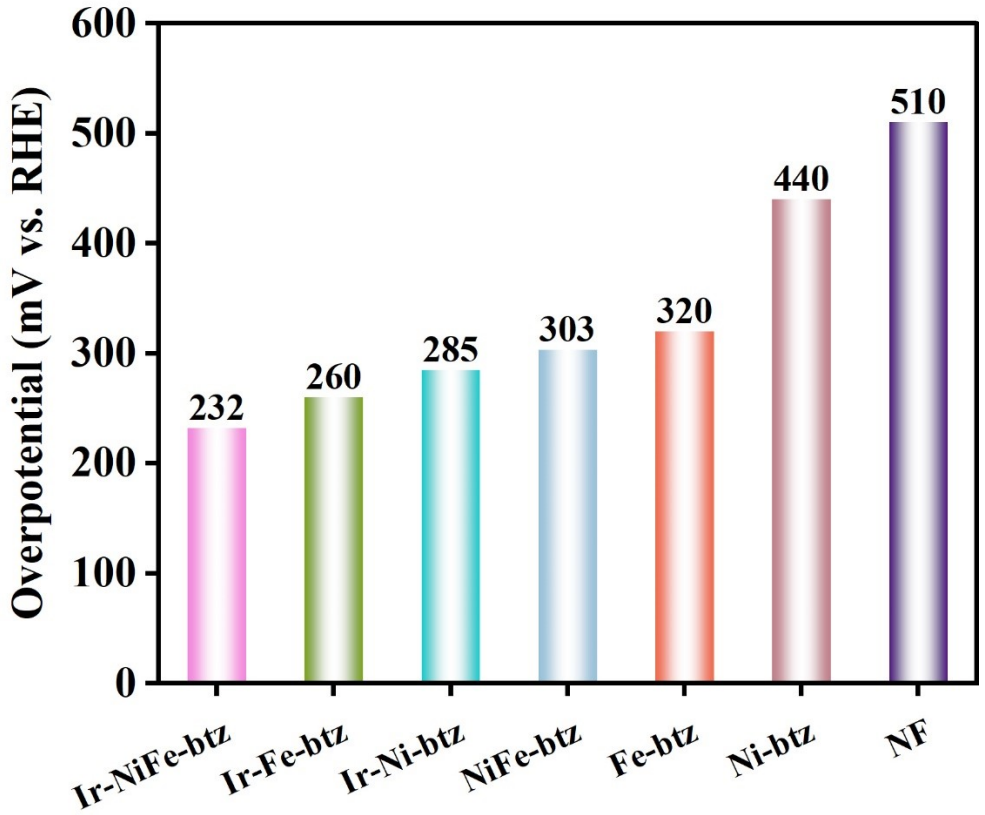

Figure S15. Histograms of the overpotentials at 100 mA cm^{-2} for various electrodes.

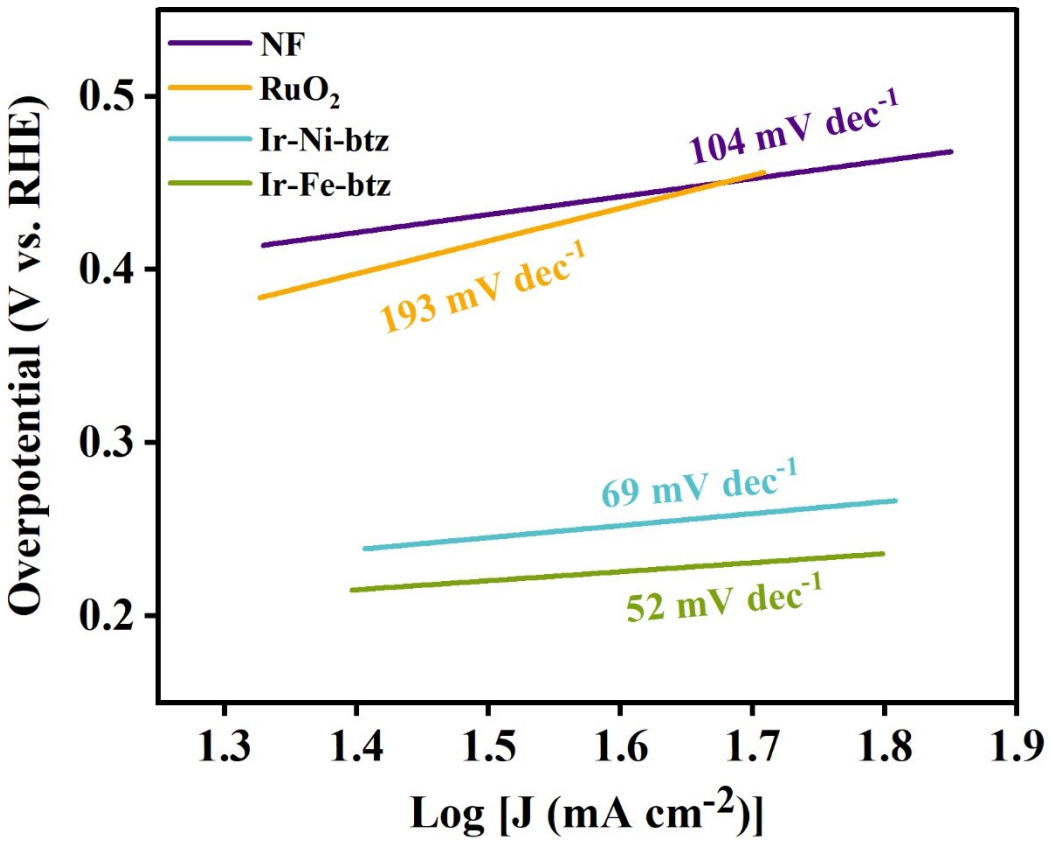

Figure S16. Tafel plots of Ir-Fe-btz, Ir-Ni-btz, NF and RuO_2.

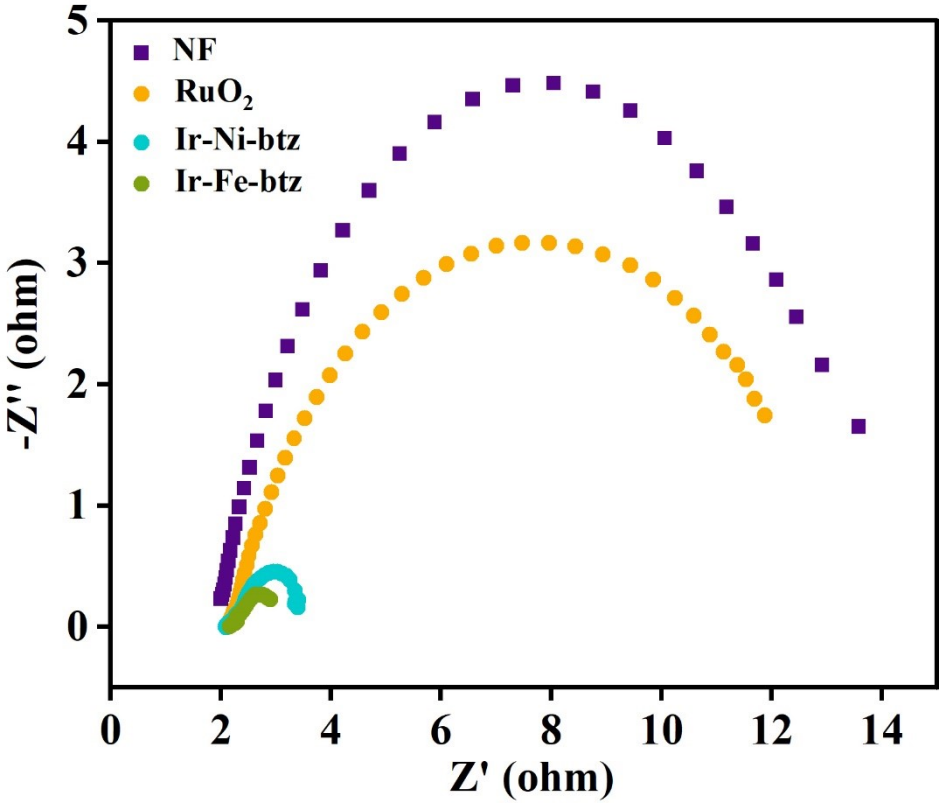

Figure S17. Nyquist plots of Ir-Fe-btz, Ir-Ni-btz, NF and RuO_2.

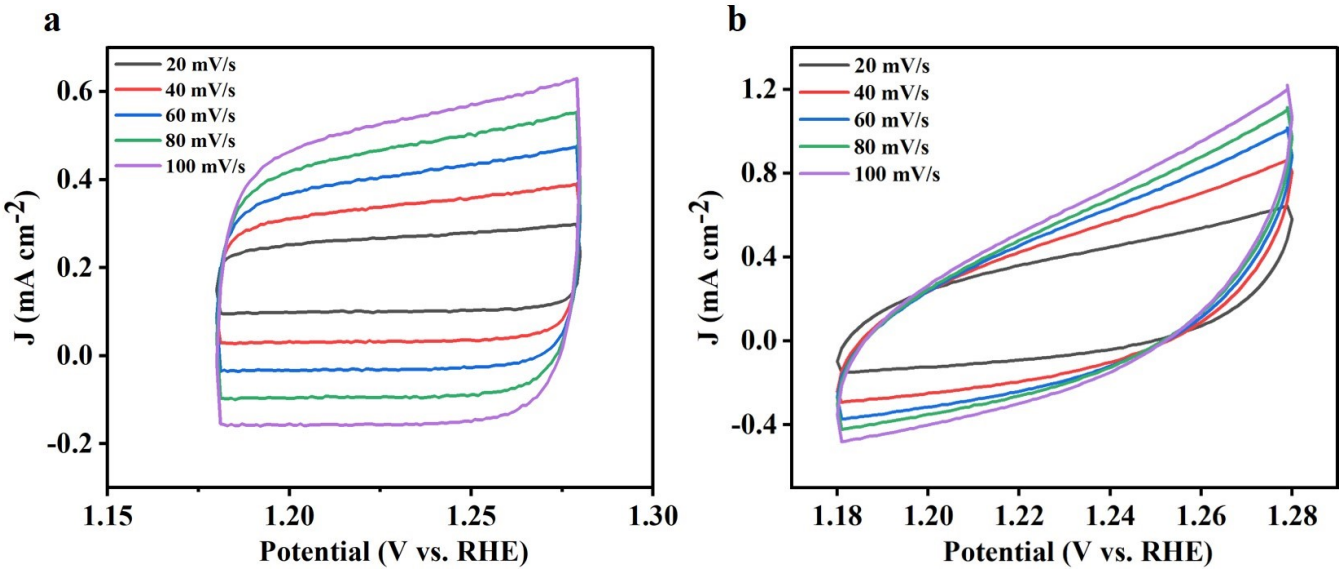

Figure S18. Cyclic voltammograms of **a)** bare NF and **b)** RuO_2 recorded in the non-Faradic region (1.18-1.28 V vs. RHE) at different scan rates.

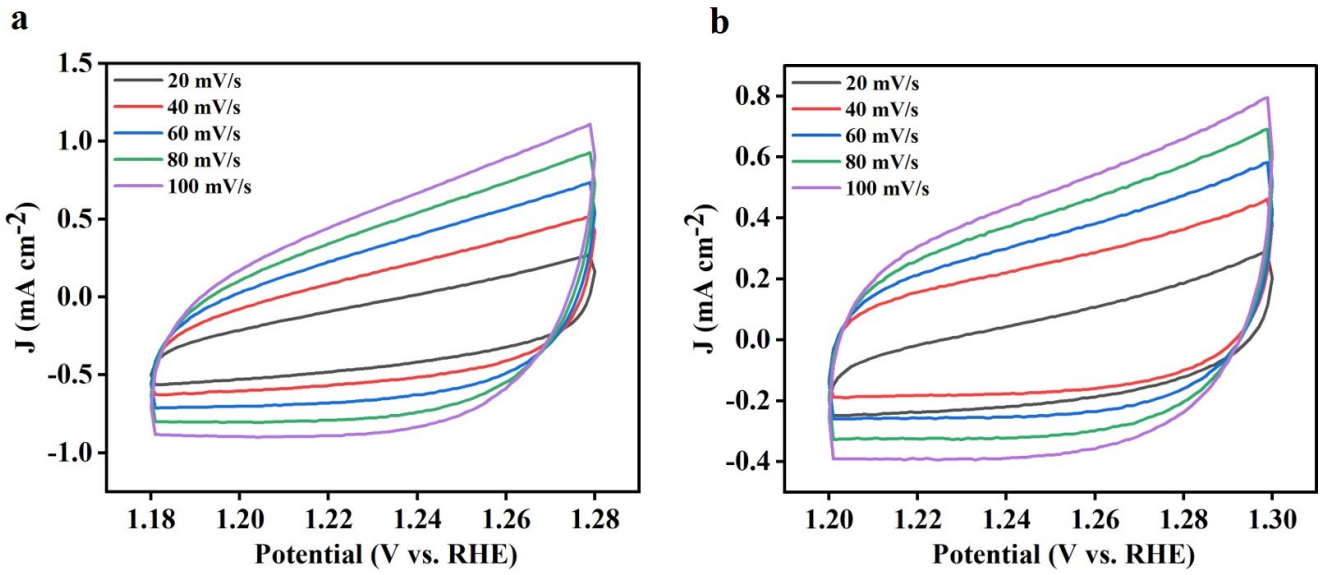

Figure S19. Cyclic voltammograms of **a)** Ni-btz/NF and **b)** Fe-btz/NF recorded in the non-Faradic region (1.18-1.28 V vs. RHE) at different scan rates.

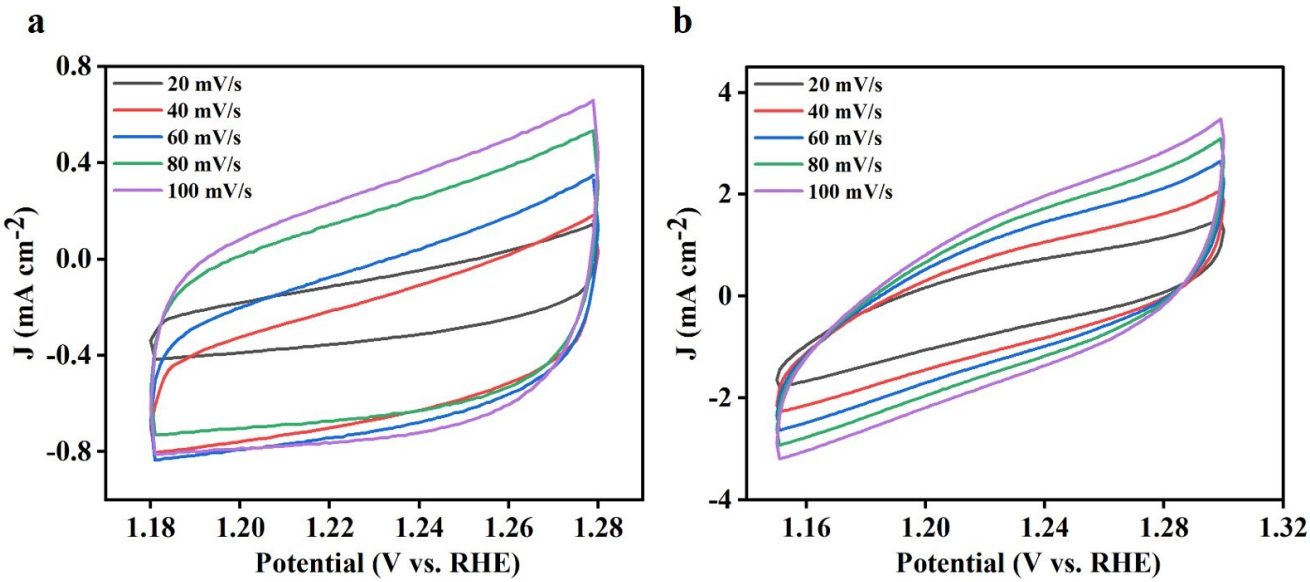

Figure S20. Cyclic voltammograms of **a)** NiFe-btz/NF and **b)** Ir-NiFe-btz/NF recorded in the non-Faradic region (1.18-1.28 V vs. RHE) at different scan rates.

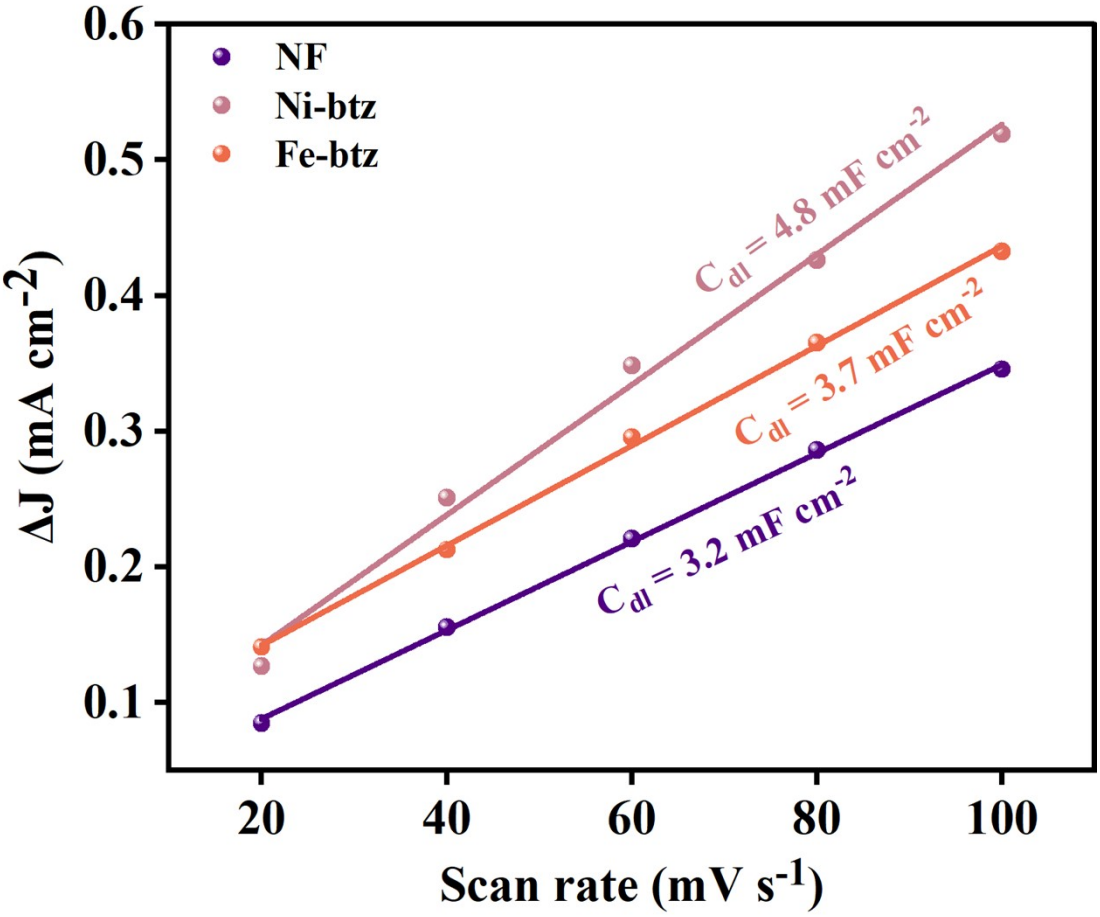

Figure S21. Double-layer capacitance (C_{dl}) value of bare NF, Ni-btz/NF, and Fe-btz/NF electrodes.

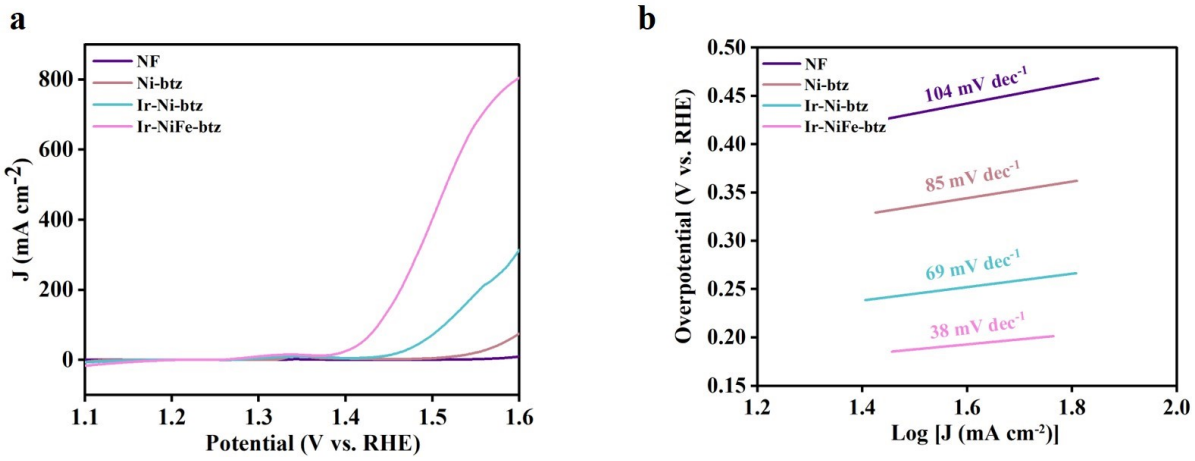

Figure S22. **a)** LSV curves and **b)** Tafel slopes of monometallic Ir-Ni-btz/NF electrode compared with bimetallic Ir-NiFe-btz/NF.

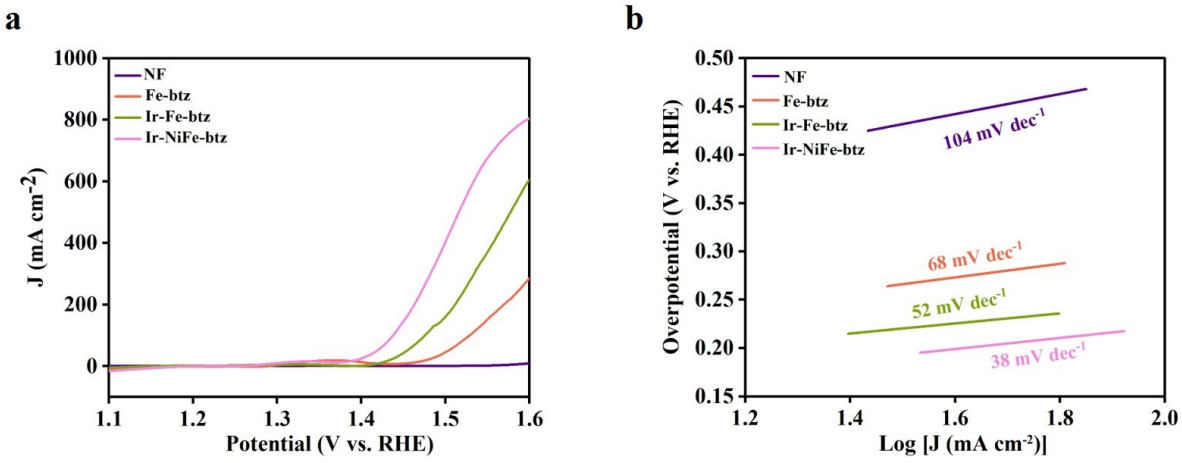

Figure S23. **a)** LSV curves and **b)** Tafel slopes of monometallic Ir-Fe-btz/NF electrode compared with bimetallic Ir-NiFe-btz/NF.

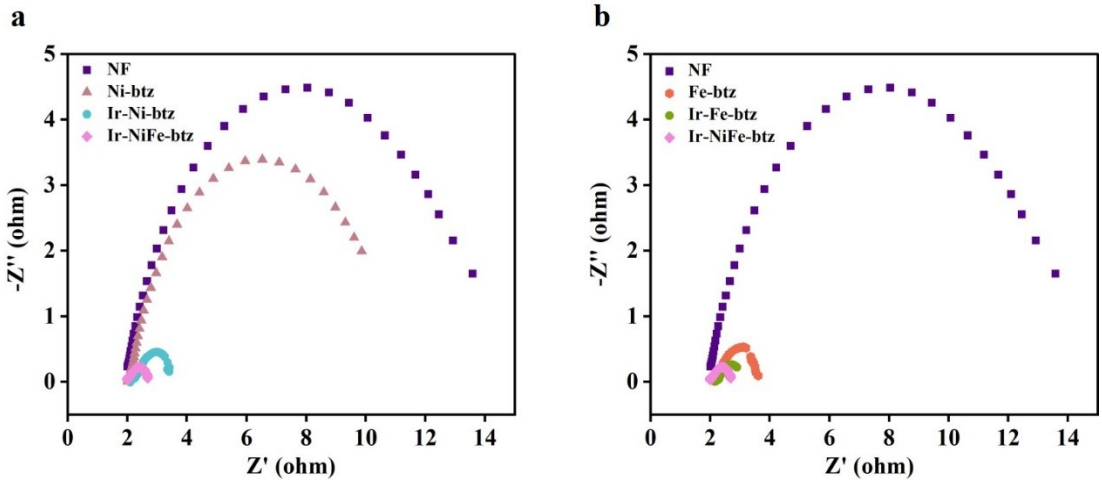

Figure S24. Nyquist plots of **a)** monometallic Ir-Ni-btz/NF and **b)** monometallic Ir-Fe-btz/NF electrodes compared with bimetallic Ir-NiFe-btz/NF.

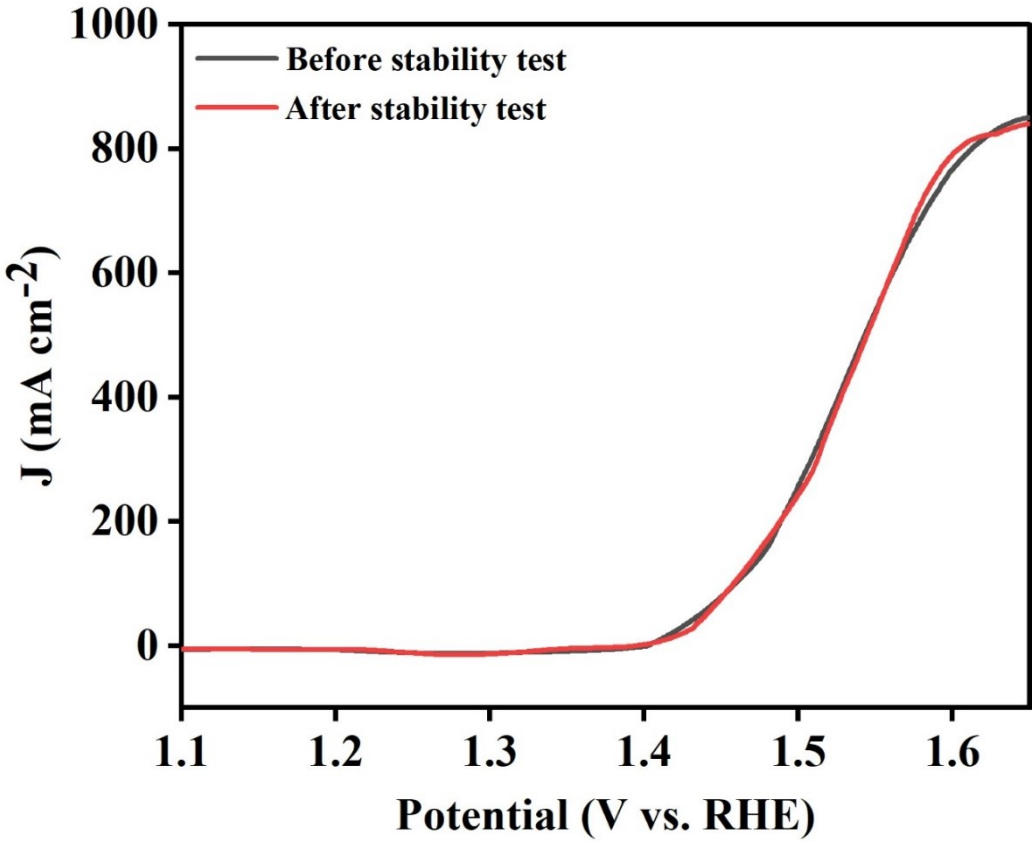

Figure S25. LSV curves of Ir-NiFe-btz/NF electrode before and after 100-hour stability test.

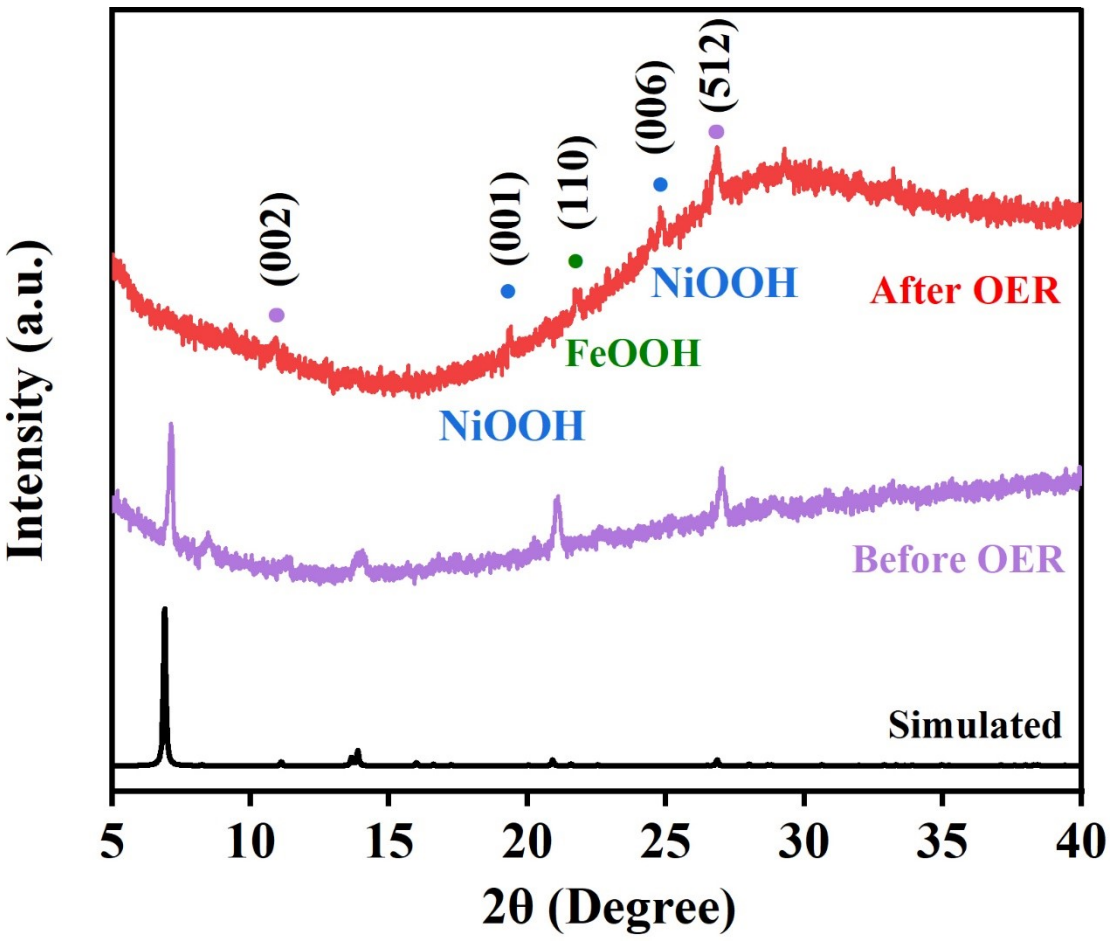

Figure S26. PXRD pattern of post-Ir-NiFe-btz/NF.

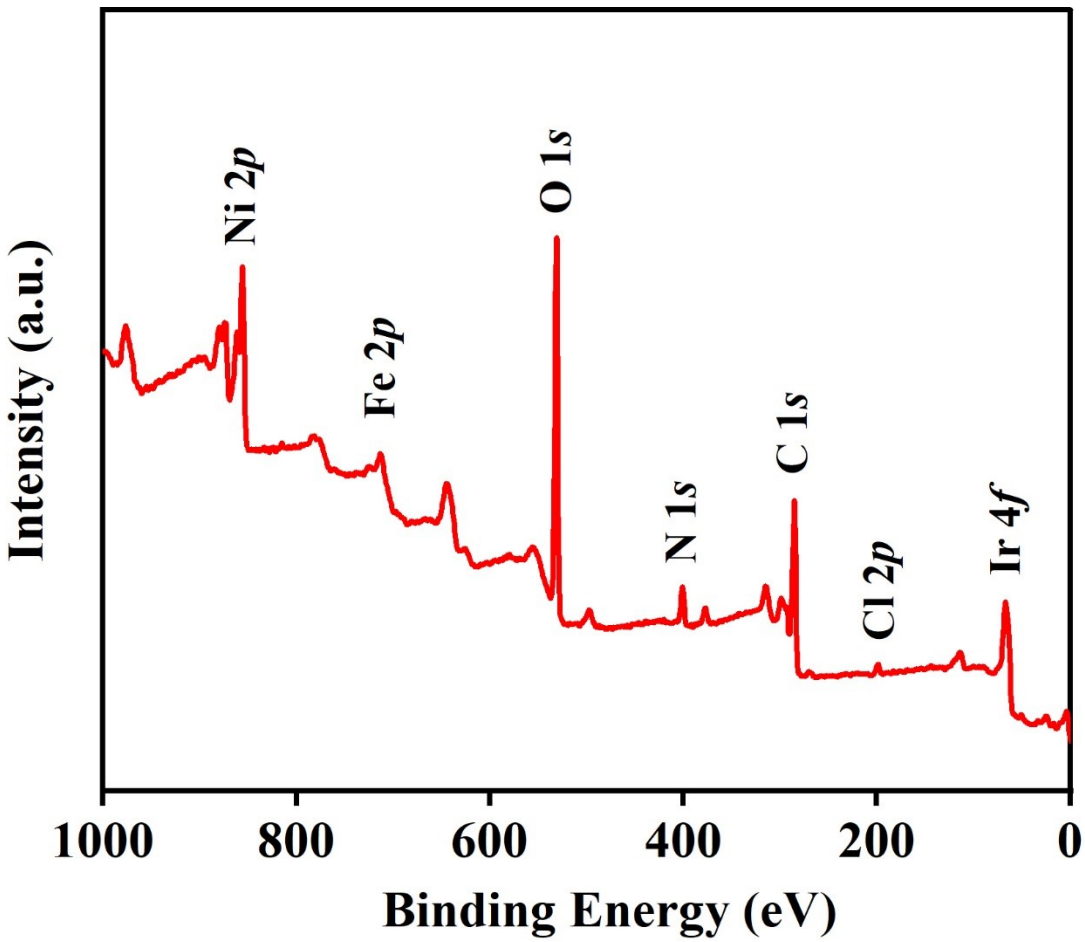

Figure S27. XPS survey spectrum of post-Ir-NiFe-btz.

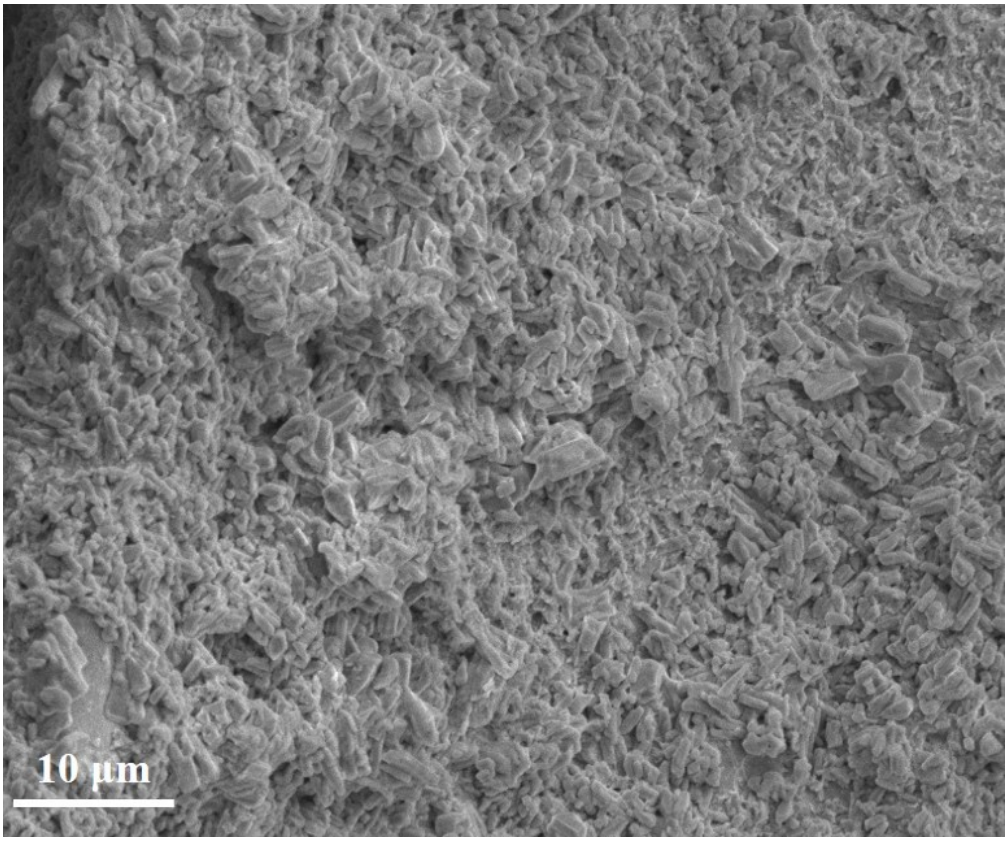

Figure S28. SEM image of post-Ir-NiFe-btz.

Table S1: OER performance comparisons between this work and previously reported NiFe-MOF-based and Ir-based electrocatalysts.

	Overpotential at 10 mA cm^{-2} (mV)	Tafel (mV dec^{-1})	References
Ir-NiFe-btz	182	38	This work
NiFe-MOF-74	227	72	[1]
$NiFe_{0.33}$-MOF	230	61	[2]
NiFc-MOF	217	58	[3]
c/a-NiFe-MOF	236	40	[4]
Ir-NiFe-LDH	246	48.6	[5]
Ir@Ni-NDC	210	44.7	[6]
Ir-Ni-NS	270	70	[7]
Ir-$Ni(OH)_2$	248	75.5	[8]
Ir-Co_3O_4@NC	225	64	[9]
Ir-NR/C	296	60.3	[10]

References:

1. Y. Guan, T. Liu, Y. Wu, X. Chu, B. Liu, N. Zhang, G. Che, W. Jiang and C. Liu, Self-reconstruction in self-supporting MOF-74 electrode to enhance electrocatalytic oxygen evolution, *Int. J. Hydrogen Energ*. 2024, **55**, 796-804.

2. X. Liu, S. Su, H. Yin, S. Zhang, T. T. Isimjan, J. Huang, X. Yang and D. Cai, Precise Anchoring of Fe Sites by Regulating Crystallinity of Novel Binuclear Ni-MOF for Revealing Mechanism of Electrocatalytic Oxygen Evolution, *Small*, 2024, **20**, 2306085.

3. T. Ren, J. Wang, X. Yu, Y. Chen, Y. Wu, G. Che, W. Jiang, H. Teng and C. Liu, The electrocatalytic self-reconstruction of ultrathin 2D MOF nanoarrays supported on alloy foam improves the oxygen evolution reaction, *Colloid Surface A.* 2024, **684**, 133136.

4. Y. Li, W. Ma, H. Yang, Q. Tian, Q. Xu and B. Han, CO 2-Assisted synthesis of a crystalline/amorphous NiFe-MOF heterostructure for high-efficiency electrocatalytic water oxidation, *Chem. Commun.* 2022, **58**, 6833-6836.

5. S. Jung, R. A. Senthil, A. Min, A. Kumar, C. J. Moon, G. H. Jeong, T. W. Kim and M. Y. Choi, Exploring Ir-doped NiFe-LDH nanosheets via a pulsed laser for oxygen evolution kinetics: in situ Raman and DFT insights, *J. Mater. Chem. A* 2024.

6. J. Yang, Y. Shen, Y. Sun, J. Xian, Y. Long and G. Li, Ir nanoparticles anchored on metal-organic frameworks for efficient overall water splitting under pH-universal conditions, *Angew. Chem. Int. Ed. Engl.* 2023, **135**, e202302220.

7. Q. Jiang, J. Xu, Z. Li, C. Zhou, X. Chen, H. Meng, Y. Han, X. Shi, C. Zhan and Y. Zhang, Two-dimensional metal-organic framework nanosheet supported noble metal nanocrystals for high-efficiency water oxidation, *Adv. Mater. Inter.* 2021, **8**, 2002034.

8. R. Guo, W. Shi, W. Liu, X. Yang, Y. Xie, T. Yang and J. Xiao, Ultralow noble metals doping enables metal-organic framework derived Ni (OH) 2 nanocages as efficient water oxidation electrocatalysts, *Chem. Engin. J.* 2022, **429**, 132478.

9. Y. Xie, Y. Su, H. Qin, Z. Cao, H. Wei, F. Wu and G. Ou, Ir-doped Co3O4 as efficient electrocatalyst for acidic oxygen evolution reaction, *Int. J. Hydrogen Energ*. 2023, **48**, 14642-14649.

10. F. Luo, L. Guo, Y. Xie, J. Xu, K. Qu and Z. Yang, Iridium nanorods as a robust and stable bifunctional electrocatalyst for pH-universal water splitting, *Appl. Catal. B-Environ.* 2020,

279, 119394.